

# $W\gamma$ and $Z\gamma$ production and limits on anomalous $WW\gamma$ , $ZZ\gamma$ and $Z\gamma\gamma$ couplings with D0 detector

Xuebing Bu

Fermi National Accelerator Laboratory, Batavia, Illinois 60510, USA  
xbbu@fnal.gov

May 8, 2012

The recent D0 results on  $W\gamma$  and  $Z\gamma$  production are presented. First, the cross section and the difference in rapidities between photons and charged leptons for inclusive  $W(\rightarrow l\nu)+\gamma$  production in  $e\gamma$  and  $\mu\gamma$  final states are discussed, then are the cross section and differential cross section as a function of photon transverse momentum for  $Z\gamma \rightarrow l^+l^-$  ( $l = e, \mu$ ) process. Finally, I present the limits on anomalous  $WW\gamma$ ,  $ZZ\gamma$  and  $Z\gamma\gamma$  couplings.

## 1 Introduction

The electroweak component of standard model (SM) has been remarkably successful in describing experimental results. The self-interaction of the gauge bosons (the  $W$ , the  $Z$ , and the photon) is a consequence of the non-Abelian  $SU(2)_L \times U(1)_Y$  gauge symmetry of the SM. The gauge boson self-interactions appear as vertices involving three gauge bosons, and result in the production of pairs of bosons. The  $WW\gamma$ ,  $ZZ\gamma$  and  $Z\gamma\gamma$  vertices are examples for that self-interactions of gauge bosons, and very sensitive to new physics. For instance, we could use the process  $p\bar{p} \rightarrow W\gamma \rightarrow l\nu\gamma$  ( $l = e, \mu$ ) to study the  $WW\gamma$  vertex, and search for any anomalous departure from SM  $WW\gamma$  coupling. In particular, because the  $Z$  boson carries no electric charge, a coupling between a  $Z$  boson and a photon is not permitted in SM.

In this review we summarize recent D0 results in measurements of cross section and the difference in rapidities between photons and leptons for inclusive  $W(\rightarrow l\nu) + \gamma$  ( $l = e, \mu$ ) production, and the cross section and differential cross section as a function of photon momentum for  $Z\gamma \rightarrow l^+l^-$  ( $l = e, \mu$ ) production, as well as the limits on anomalous  $WW\gamma$ ,  $ZZ\gamma$  and  $Z\gamma\gamma$  couplings [1, 2].

## 2 The D0 detector

The D0 detector is a multi-purpose particle detector. It has been constructed to study proton-antiproton collisions at a center of mass energy  $\sqrt{s} = 1.96$  TeV. The D0 detector [3] comprises a central tracking system in a 2 T superconducting solenoidal magnet, surrounded by a central preshower (CPS) detector, a liquid-argon sampling calorimeter, and an outer muon system. Fig. 1 is the overview of D0 detector. The tracking system, a silicon microstrip tracker (SMT) and a scintillating fiber tracker (CFT), provides coverage for charged particles in the pseudorapidity range  $|\eta| < 3$  [4]. The CPS is located immediately before the inner layer of the calorimeter, and has about one radiation length of absorber, followed by several layers of scintillating strips. The calorimeter consists of a central sector (CC) with coverage of  $|\eta| < 1.1$ , and two end calorimeters (EC) covering up to  $|\eta| \approx 4.2$ . The electromagnetic (EM) section of the calorimeter is segmented into four longitudinal layers (EM*i*, *i* = 1, 4) with transverse segmentation of  $\Delta\eta \times \Delta\phi = 0.1 \times 0.1$  [4], except in EM3, where it is  $0.05 \times 0.05$ . The muon system resides beyond the calorimeter and consists of a layer of tracking detectors and scintillation trigger counters before 1.8 T iron toroidal magnet, followed by two similar layers after the toroid. The coverage of the muon system corresponds to  $|\eta| < 2$ . Luminosity is measured using plastic scintillator arrays located in front of the EC cryostats, covering  $2.7 < |\eta| < 4.4$ . The data acquisition system consists of a three-level trigger, designed to accommodate the high instantaneous luminosity.

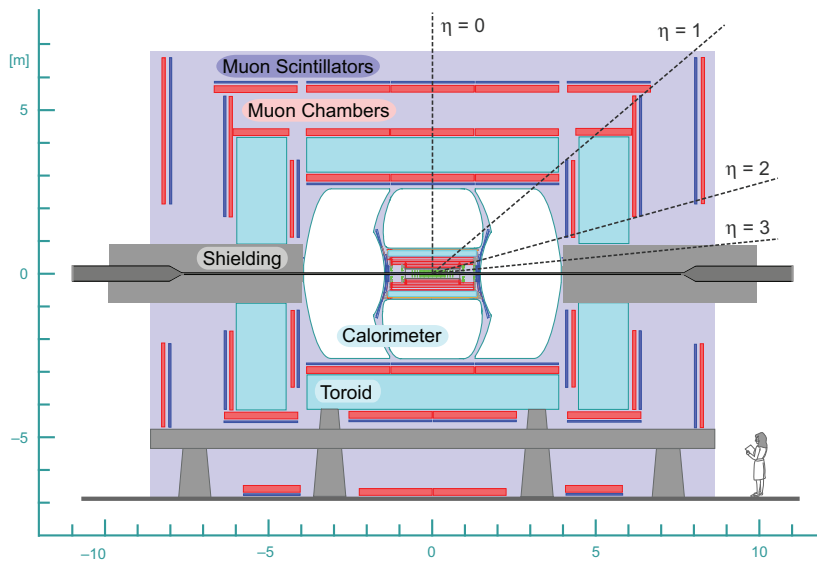


Figure 1: (color online). The D0 Detector.

### 3 $W\gamma$ production

In the SM, tree level production of a photon in association with a  $W$  boson occurs due to prompt  $W\gamma$  production via the diagrams shown in Fig. 2 or via final state radiation (FSR), where a lepton from the  $W$  boson decay radiates a photon (shown in Fig. 3). At leading order (LO) of SM prediction, the interference between the amplitudes in Fig. 2 produces a zero in the total  $W\gamma$  yield at a specific angle  $\theta^*$  between the  $W$  boson and the incoming quark [5] in the  $W\gamma$  rest frame (see Fig. 4). Since in hadronic collisions the longitudinal momenta of neutrinos from  $W$  decay cannot be measured, the angle  $\theta^*$  at which the radiation amplitude is zero is difficult to measure directly. However, the radiation amplitude zero (RAZ) is also visible in the charge-signed photon-lepton rapidity difference as a dip around  $-1/3$  [6] (see Fig. 5).

In this review, I present the measurements of the cross section and the distribution of the charge-signed rapidities difference between photon and lepton using data corresponding to an integrated luminosity of  $4.2 \text{ fb}^{-1}$  collected by D0 detector at the Fermilab Tevatron Collider.

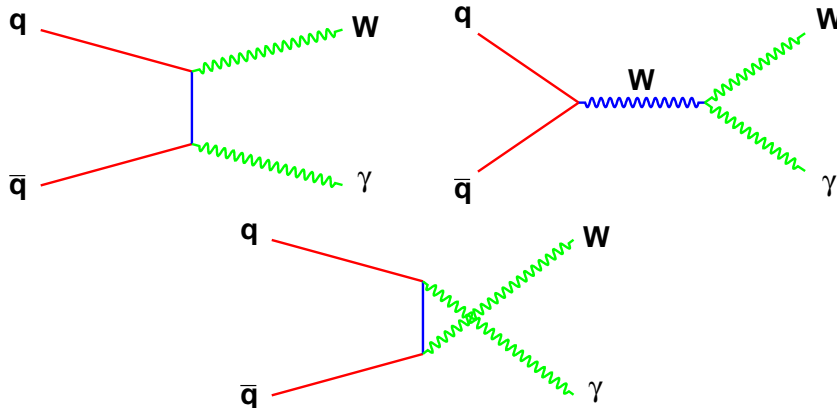


Figure 2: (color online). Feynman diagrams for prompt  $W\gamma$  production.

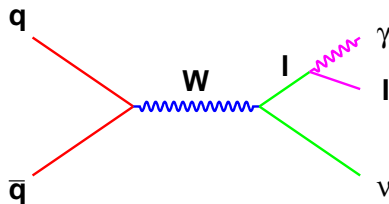


Figure 3: (color online). Feynman diagram for  $W\gamma$  production via final state radiation.

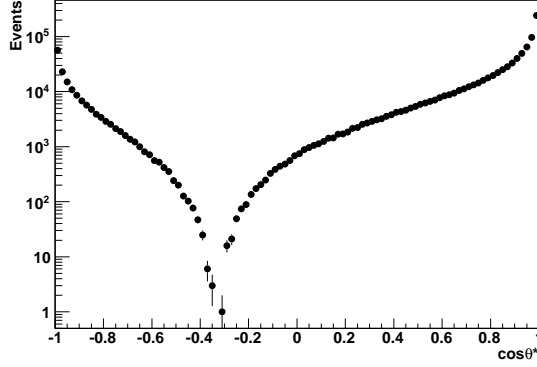


Figure 4:  $\cos\theta^*$  between the  $W$  and incoming quark in  $W\gamma$  rest frame from PYTHIA [7].

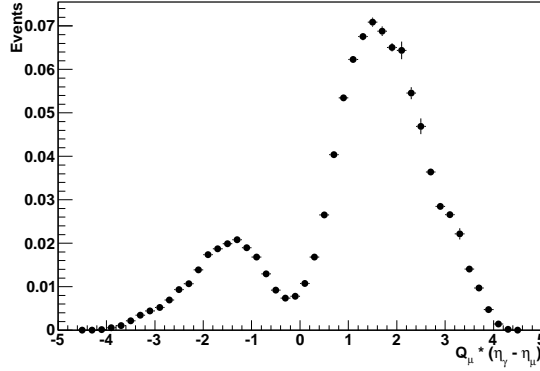


Figure 5: Charge-signed photon-lepton rapidity difference from next-to-leading order  $W\gamma$  generator [6, 8]

### 3.1 Event selection

For the electron channel with the  $W$  boson decaying into an electron and a neutrino, a suite of single-electron triggers are used to collect the candidate events. The electrons are selected by requiring an EM cluster in either the CC ( $|\eta| < 1.1$ ) or EC ( $1.5 < |\eta| < 2.5$ ) with transverse momentum  $p_T > 25$  GeV. Electron candidates are required to be isolated in both the calorimeter and the tracker, have a shower shape consistent with that of an electron, and a spatial match to a track. Further a multivariate likelihood discriminant and an artificial

neural network are used to further reject background from jets misidentified as electrons. To suppress the  $Z/\gamma^* \rightarrow ee$  background, the event missing transverse energy,  $\cancel{E}_T$ , must exceed 25 GeV, the transverse mass of the  $W$  boson,  $M_T$ , must exceed 50 GeV and the azimuthal angle between the electron and photon is required to be  $\Delta\phi_{e\gamma} < 2$ .

For the muon channel with the  $W$  boson decaying into an muon and a neutrino, a suite of single-muon triggers are used to collect the candidate events. The muons are required to be within  $|\eta| < 1.6$ , isolated in both the tracker and the calorimeter, and matched to a track with transverse momentum  $p_T > 20$  GeV. To suppress the  $Z/\gamma^* \rightarrow \mu\mu$  background, the  $\cancel{E}_T$  in the event must exceed 20 GeV,  $M_T$  must exceed 40 GeV, and there must be no additional muons or tracks with  $p_T > 15$  GeV.

The photon candidates in both the electron and muon channels are required to have transverse momentum  $p_T^\gamma > 15$  GeV. In addition, photon candidates are required to be either in the CC ( $|\eta| < 1.1$ ) or EC ( $1.5 < |\eta| < 2.5$ ), and be isolated in both the calorimeter and the tracker. Furthermore, the output of an artificial neural network ( $O_{NN}$ ) [9], that combines information from a set of variables sensitive to differences between photons and jets in the tracking detector, the calorimeter, and the CPS detector, is required to be larger than 0.75.

To suppress background from FSR, the photon and the lepton must be separated by  $\Delta R_{l\gamma} > 0.7$ , and the three-body transverse mass (see Eq. 1) of the photon, lepton, and missing transverse energy must exceed 110 GeV.

$$M_T^{l\gamma\cancel{E}_T} = \sqrt{(\sqrt{M_{l\gamma}^2 + |\mathbf{p}_T(\gamma) + \mathbf{p}_T(l)|^2} + \cancel{E}_T)^2 - |\mathbf{p}_T(\gamma) + \mathbf{p}_T(l) + \cancel{E}_T|^2} \quad (1)$$

## 3.2 Backgrounds

There are four major sources of background in this analysis: (i) events with  $el + X$  final state, where the electron is misidentified as photon due to tracking inefficiency; (ii)  $W$ +jet production, where the jet is misidentified as the photon; (iii)  $Zll\gamma$  production, where one of the lepton is lost; (iv)  $W_{\tau\nu}\gamma$  production, where  $\tau$  further decays to  $e$  or  $\mu$ .

The  $el + X$  background is composed of events where the electron is misidentified as a photon due to tracking inefficiencies, and mainly comes from the di-boson production. To estimate its contribution, an orthogonal data sample is selected by requiring the EM cluster be matched with a good track. Then the ratio for EM cluster matching a good track and passing the photon no-track requirement is measured from the  $Z \rightarrow ee$  data with parameterizing as a function of  $\eta$ . Finally, the  $el + X$  contribution is calculated with multiplying the ratio on the orthogonal sample.

The dominant background for this analysis is  $W$ +jet production. Two different data driven methods have been used to estimate the contribution. In method one, an orthogonal data sample ( $W$ +bad photon) is selected by reversing the photon track isolation or shower width requirement. Then the ratio of

jet passing the good photon selection criteria and failing the track isolation or shower width requirement is measured from the di-jet data. This ratio is measured as a function of  $p_T$  in 5  $\eta$  regions for photon in CC and EC respectively. The final W+jet contribution is obtained with applying these ratios to the selected W+bad photon data events. In method two, a fit is performed on the photon  $O_{NN}$  distributions in 5  $\eta$  regions for photon in CC and EC respectively. The photon  $O_{NN}$  templates are obtained from photon and jet Monte Carlo (MC) simulation, since the  $O_{NN}$  is well modelled [9, 10]. The results from these two methods are consistent, considering the poor statistics of template fitting method, the results from reversing photon quality cuts is used as the default.

Small backgrounds from  $Z_{ll} + \gamma$ , where one of the leptons from Z decays is lost, and  $W_{\tau\nu} + \gamma$ , where the  $\tau$  decays to a  $e$  or  $\mu$ , are estimated from PYTHIA Drell-Yan  $Z/\gamma^* \rightarrow \mu\mu$  and  $W_{\tau\nu} + \gamma$  MC respectively.

### 3.3 Signal

The signal is simulated using the Baur and Berger LO event generator [11], interfaced to PYTHIA [7] for subsequent parton showering and hadronization. To avoid the double counting of the FSR events, the diagram corresponding to FSR of photons is disabled in PYTHIA. The shape and normalization of the signal  $p_T^\gamma$  spectrum are reweighted to the next-to-leading order (NLO) prediction [8]. The acceptance of the kinematic and geometric requirements for this analysis is calculated using this  $p_T^\gamma$ -weighted signal MC. All MC events are generated using the CTEQ6L1 [12] parton distribution functions (PDF), followed by a GEANT [13] simulation of the D0 detector.

### 3.4 Systematic uncertainties and results

The dominant systematic uncertainties considered in this analysis are:

- 6.1% uncertainty on the total luminosity;
- 5% uncertainty on the single lepton trigger efficiency;
- 3% uncertainty on the photon identification;
- 3% uncertainty on the lepton identification;
- 0.9% uncertainty on the track veto;
- $\sim 10$  % uncertainty on estimation of W+jet background.

The number of predicted and observed events in both the electron and muon channels are summarized in Table 1.

The cross section multiplied by the branching fraction for the process  $p\bar{p} \rightarrow W\gamma + X \rightarrow l\nu\gamma + X$  is measured to be  $7.6 \pm 0.4$  (stat.)  $\pm 0.6$  (syst.) pb, which is in good agreement with the SM expectation of  $7.6 \pm 0.2$  pb for  $E_T^\gamma > 15$  GeV and  $\Delta R_{l\gamma} > 0.7$ .

	$e\nu\gamma$ channel	$\mu\nu\gamma$ channel
$W$ +jet	$33.9 \pm 3.7$	$64.6 \pm 6.8$
$leX$	$1.1 \pm 0.6$	$2.1 \pm 0.7$
$Z\gamma \rightarrow ll\gamma$	$1.8 \pm 0.3$	$17.6 \pm 1.9$
$W\gamma \rightarrow \tau\nu\gamma$	$2.3 \pm 0.3$	$5.4 \pm 0.6$
Total background	$39.1 \pm 3.8$	$89.7 \pm 7.2$
SM $W\gamma$ prediction	$150.9 \pm 13.8$	$282.1 \pm 25.4$
Data	196	363

Table 1: Number of predicted and observed events with statistical and systematic uncertainties. (Table from Ref. [1], see text)

The charge-signed photon-lepton rapidity difference for the combined electron and muon channels is shown in Fig. 6. The events with EC electrons are excluded from Fig. 6 due to the significant charge mis-identification. The background-subtracted data are in good agreement with the SM prediction, and a  $\chi^2$  test comparing the background-subtracted data with the SM prediction yields 4.6 for 11 degrees of freedom.

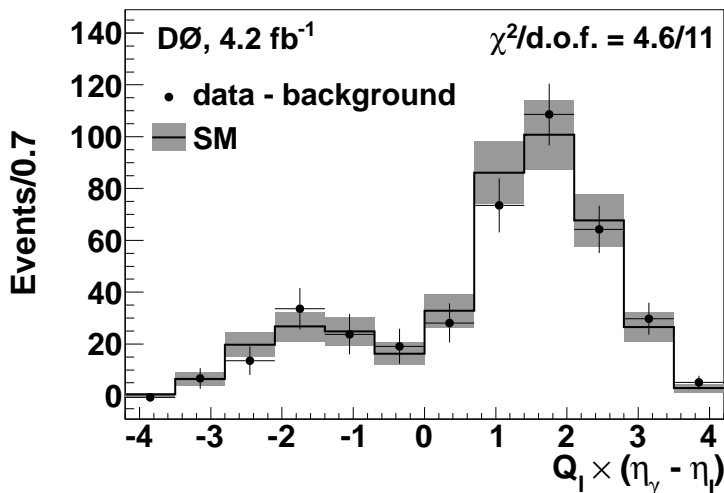


Figure 6: The charge-signed photon-lepton rapidity difference ( $Q_l \times (\eta_\gamma - \eta_l)$ , where  $Q_l$  is the charge of the lepton) in background-subtracted data compared to the SM expectation for the combined electron and muon channels. The background-subtracted data are shown as black points with error bars representing their total uncertainties. The SM signal prediction is given by the solid line, with the shaded area representing its uncertainty. (Figure from Ref. [1], see text)

## 4 $Z\gamma$ production

In the SM, production of a photon in association with a  $Z$  boson occurs due to radiation of a photon from an incoming quark (see Figs. 16(b) and 10(b)), or from final state radiation of a lepton of the outgoing  $Z$  boson (see Figs. 7(c) and 7(d)).

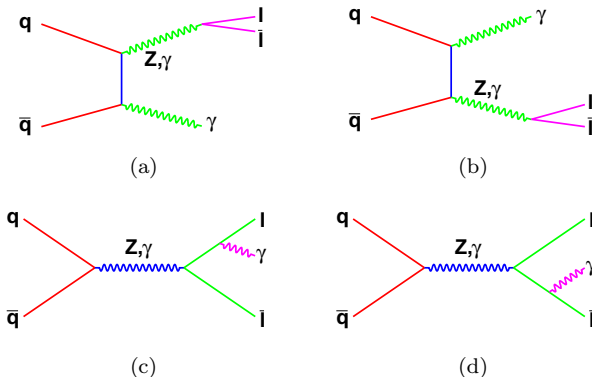


Figure 7: Feynman diagrams for the tree-level  $Z(\gamma) \rightarrow l^+l^-\gamma$  processes in SM: (a) and (b) describe the initial state radiation, (c) and (d) describe the final state radiation.

In this review, I present the measurements of the inclusive cross section and differential cross section for  $Z\gamma$  production in the electron and muon channels using a data sample corresponding to an integrated luminosity of  $6.2 \text{ fb}^{-1}$  collected at  $\sqrt{s} = 1.96 \text{ TeV}$  by the D0 detector at the Fermilab Tevatron Collider.

### 4.1 Event selection

For electron channel with  $Z$  boson decaying to two electrons, the same single-electron triggers and electron selection criteria as  $W\gamma$  analysis described in Section 3 is used. Two electron candidates with transverse momentum  $p_T > 15 \text{ GeV}$  are selected, and the highest  $p_T$  electron must have  $p_T > 25 \text{ GeV}$ .

For muon channel with  $Z$  boson decaying to two muons, the same single-muon triggers and muon selection criteria as  $W\gamma$  analysis is used, except the  $\eta$  coverage is extended to 2. Two muon candidates with transverse momentum  $p_T > 15 \text{ GeV}$  are selected, and the highest  $p_T$  muon must have  $p_T > 20 \text{ GeV}$ .

Photon candidates in both electron and muon channels are required to be in CC and have transverse momentum  $p_T > 10 \text{ GeV}$ . By comparison with  $W\gamma$  analysis, same photon selection criteria are used, except the  $O_{NN}$  is required to be greater than 0.1 instead of 0.75.

In addition, the dilepton invariant mass,  $M_{ll}$ , is required to be greater than 60 GeV, and the photon must be separated from each lepton by  $\Delta R_{l\gamma} > 0.7$ . In the end, 1002 and 1000 data events are selected in electron and muon channels respectively. In order to reduce the contribution of FSR, subset data samples

are defined with the requirement that the reconstructed three-body invariant mass,  $M_{ll\gamma}$ , exceed 110 GeV. With this additional requirement, 304 and 308 data events are selected in the electron and muon channels, respectively.

## 4.2 Background

The dominant background for this analysis is the  $Z$ +jet, where the jet is misidentified as a photon. For electron channel, same as  $W\gamma$  analysis, the  $Z$ +jet background is estimated from an orthogonal data sample by reversing the photon quality cuts. For muon channel, a  $2 \times 2$  matrix method is used to estimate the  $Z$ +jet background contribution. The  $Z$ +jet background is also estimated through a fit to the shape of the  $O_{NN}$  distributions in data for both electron and muon channels. The results are in good agreement with those obtained from the reversing and matrix methods.

## 4.3 Total cross section

To eliminate the uncertainties of lepton trigger efficiencies, reconstruction efficiencies and integrated luminosity, the total cross section for  $ll\gamma$  production is obtained from the ratio of the acceptance-corrected  $ll\gamma$  rate for  $M_{ll} > 60$  GeV,  $\Delta R_{ll\gamma} > 0.7$ ,  $p_T^\gamma > 10$  GeV/ $c$ , and  $|\eta^\gamma| < 1$ , to the total acceptance-corrected dilepton rate for  $M_{ll} > 60$  GeV. Thus the total cross section for  $Z\gamma$  is estimated using the ratio to multiply the inclusive  $Z/\gamma^* \rightarrow ll$  production theoretical cross section:

$$\sigma_{Z\gamma} = \frac{\kappa \cdot N_{ll\gamma}^{\text{data}} \cdot (A \times \epsilon_{ID})_{ll\gamma}^{-1}}{N_{ll}^{\text{data}} \cdot (A \times \epsilon_{ID})_{ll}^{-1}} \times \sigma_Z \quad (2)$$

Here,  $N_{ll}^{\text{data}}$  and  $N_{ll\gamma}^{\text{data}}$  are the number of selected  $Z$  and background-subtracted  $Z\gamma$  events in data sample, respectively. The  $\sigma_Z$  is the theoretical cross section for inclusive  $Z/\gamma^* \rightarrow ll$  production. The factor  $\kappa$  corrects for the detector resolution effects that would cause events not to pass the selections on the generator-level quantities, but to pass the reconstruction requirements, where the photon energy resolution in the low  $p_T$  is the dominant source. The factors  $(A \times \epsilon_{ID})_{ll\gamma}$  and  $(A \times \epsilon_{ID})_{ll}$  provide the fraction of events that pass the analysis requirements, with all acceptances measured relative to the kinematic requirements at the generator level for the  $ll\gamma$  and  $ll$  final states, respectively. The PYTHIA  $Z/\gamma^* \rightarrow ll$  events are used to calculate the  $A \times \epsilon_{ID}$  after reweighting the  $p_T^Z$  spectrum to the observed one.

The total cross section has been measured with and without the  $M_{ll\gamma} > 110$  GeV requirement to reflect the FSR effect. The corresponding results are shown in Tables 2 and 3. The measured cross section are consistent with the NLO MCFM [14].

Table 2: Summary of the total cross-section measurements, when no  $M_{\ell\ell\gamma}$  requirement is applied, for individual channels, combined channels, and the NLO MCFM calculation with associated PDF and scale uncertainties. (Table from Ref. [2], see text)

	$\sigma_{Z\gamma} \times \mathcal{B}$ [fb]
$ee\gamma$ data	$1026 \pm 62$ (stat.) $\pm 60$ (syst.)
$\mu\mu\gamma$ data	$1158 \pm 53$ (stat.) $\pm 70$ (syst.)
$\ell\ell\gamma$ combined data	$1089 \pm 40$ (stat.) $\pm 65$ (syst.)
NLO MCFM	$1096 \pm 34$ (PDF) $^{+2}_{-4}$ (scale)

Table 3: Summary of the total cross-section measurements, with the  $M_{\ell\ell\gamma} > 110$  GeV/ $c^2$  requirement, for individual channels, combined channels, and the NLO MCFM calculation with associated PDF and scale uncertainties. (Table from Ref. [2], see text)

	$\sigma_{Z\gamma} \times \mathcal{B}$ [fb]
$ee\gamma$ data	$281 \pm 17$ (stat.) $\pm 11$ (syst.)
$\mu\mu\gamma$ data	$306 \pm 28$ (stat.) $\pm 11$ (syst.)
$\ell\ell\gamma$ combined data	$288 \pm 15$ (stat.) $\pm 11$ (syst.)
NLO MCFM	$294 \pm 10$ (PDF) $^{+1}_{-2}$ (scale)

#### 4.4 Differential cross section $d\sigma/dp_T^\gamma$

The matrix inversion technique [15] is used to extract the differential cross section  $d\sigma/dp_T^\gamma$  as a function of the true  $p_T^\gamma$ . The PYTHIA  $Z\gamma$  events are used to assemble the smearing matrix between true and reconstructed  $p_T^\gamma$ . In the end, the matrix is inverted to obtain the unsmear spectrum. The measured differential cross sections  $d\sigma/dp_T^\gamma$  are shown in Figs. 8 and 9 for no  $M_{\ell\ell\gamma}$  requirement and  $M_{\ell\ell\gamma} > 110$  GeV, respectively. The values associated with Figs. 8 and 9 are given in Tables 4 and 5. The measured cross section are good consistent with NLO MCFM.

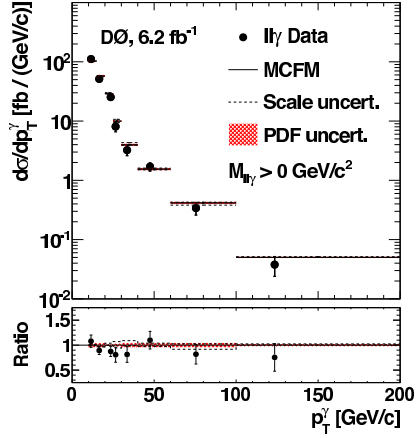


Figure 8: Unfolded  $d\sigma/dp_T^\gamma$  distribution with no  $M_{l\gamma}$  requirement for combined electron and muon data compared to the NLO MCFM prediction. (Figure from Ref. [2], see text)

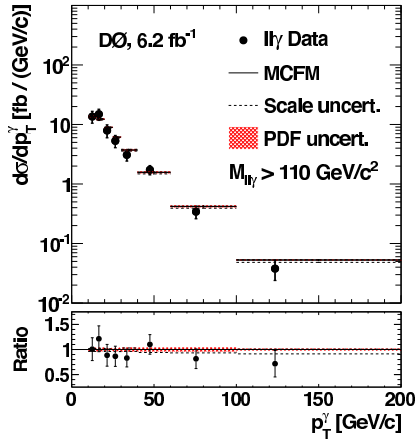


Figure 9: Unfolded  $d\sigma/dp_T^\gamma$  distribution with  $M_{l\gamma} > 110 \text{ GeV}/c^2$  for combined electron and muon data compared with the NLO MCFM prediction. (Figure from Ref. [2], see text)

Table 4: Summary of the unfolded differential cross section  $d\sigma/dp_T^\gamma$ , when no  $M_{\ell\ell\gamma}$  requirement is applied, and NLO MCFM predictions with PDF and scale uncertainties. (Table from Ref. [2], see text)

		$\ell\ell\gamma$ Combined Data		NLO MCFM	
$p_T^\gamma$ bin [GeV/c]	$p_T^\gamma$ center [GeV/c]			$d\sigma/dp_T^\gamma$ [fb/(GeV/c)]	
10–15	12.4	$111.14 \pm 4.40$ (stat.) $\pm 11.99$ (syst.)		$104.02 \pm 4.10$ (PDF) $^{+1.4}_{-1.2}$ (scale)	
15–20	17.2	$51.41 \pm 3.83$ (stat.) $\pm 2.65$ (syst.)		$57.13 \pm 2.23$ (PDF) $^{+1.3}_{-1.8}$ (scale)	
20–25	22.5	$25.34 \pm 2.74$ (stat.) $\pm 1.13$ (syst.)		$28.77 \pm 0.43$ (PDF) $^{+1.1}_{-0.7}$ (scale)	
25–30	27.5	$8.08 \pm 1.45$ (stat.) $\pm 0.40$ (syst.)		$10.16 \pm 0.26$ (PDF) $^{+0.7}_{-0.5}$ (scale)	
30–40	34.4	$3.23 \pm 0.60$ (stat.) $\pm 0.17$ (syst.)		$4.15 \pm 0.16$ (PDF) $^{+0.34}_{-0.19}$ (scale)	
40–60	48.5	$1.70 \pm 0.26$ (stat.) $\pm 0.088$ (syst.)		$1.60 \pm 0.061$ (PDF) $^{+0.008}_{-0.010}$ (scale)	
60–100	76.5	$0.34 \pm 0.079$ (stat.) $\pm 0.018$ (syst.)		$0.42 \pm 0.017$ (PDF) $^{+0.028}_{-0.028}$ (scale)	
100–200	124.5	$0.038 \pm 0.014$ (stat.) $\pm 0.002$ (syst.)		$0.052 \pm 0.001$ (PDF) $^{+0.003}_{-0.001}$ (scale)	

Table 5: Summary of the unfolded differential cross section  $d\sigma/dp_T^\gamma$ , with the  $M_{\ell\ell\gamma} > 110$  GeV/ $c^2$  requirement, and NLO MCFM predictions with PDF and scale uncertainties. (Table from Ref. [2], see text)

		$\ell\ell\gamma$ Combined Data		NLO MCFM	
$p_T^\gamma$ bin [GeV/c]	$p_T^\gamma$ center [GeV/c]			$d\sigma/dp_T^\gamma$ [fb/(GeV/c)]	
10–15	13.7	$13.57 \pm 1.87$ (stat.) $\pm 2.43$ (syst.)		$13.48 \pm 0.48$ (PDF) $^{+0.25}_{-0.51}$ (scale)	
15–20	17.2	$14.87 \pm 2.17$ (stat.) $\pm 2.30$ (syst.)		$12.25 \pm 0.47$ (PDF) $^{+0.29}_{-0.36}$ (scale)	
20–25	22.0	$7.91 \pm 1.76$ (stat.) $\pm 0.81$ (syst.)		$8.94 \pm 0.25$ (PDF) $^{+0.13}_{-0.35}$ (scale)	
25–30	27.4	$5.30 \pm 1.15$ (stat.) $\pm 0.44$ (syst.)		$6.13 \pm 0.21$ (PDF) $^{+0.016}_{-0.25}$ (scale)	
30–40	34.5	$3.08 \pm 0.57$ (stat.) $\pm 0.33$ (syst.)		$3.71 \pm 0.15$ (PDF) $^{+0.012}_{-0.14}$ (scale)	
40–60	48.6	$1.73 \pm 0.26$ (stat.) $\pm 0.17$ (syst.)		$1.57 \pm 0.061$ (PDF) $^{+0.004}_{-0.094}$ (scale)	
60–100	76.5	$0.34 \pm 0.079$ (stat.) $\pm 0.019$ (syst.)		$0.42 \pm 0.017$ (PDF) $^{+0.028}_{-0.028}$ (scale)	
100–200	124.5	$0.038 \pm 0.014$ (stat.) $\pm 0.002$ (syst.)		$0.052 \pm 0.001$ (PDF) $^{+0.003}_{-0.001}$ (scale)	

## 5 Limits on anomalous $WW\gamma$ , $ZZ\gamma$ and $Z\gamma\gamma$ couplings

For  $W\gamma$  production, an effective Lagrangian parameterizes the  $WW\gamma$  couplings with two parameters,  $\kappa_\gamma$  and  $\lambda_\gamma$  [6, 8, 11], under the assumptions of electromagnetic gauge invariance, charge conjugation ( $C$ ), parity ( $P$ ) and  $CP$  conservation. The  $\kappa_\gamma$  and  $\lambda_\gamma$  couplings are related to the magnetic dipole and electric quadrupole moments of the  $W$  boson. In the SM,  $\kappa_\gamma = 1$  and  $\lambda_\gamma = 0$ , and it is customary to introduce into the notation the difference  $\Delta\kappa_\gamma \equiv \kappa_\gamma - 1$ . A form factor with a 2 TeV common scale  $\Lambda$  for each non-SM coupling parameter, is used to assure that the  $W\gamma$  cross section does not violate unitarity.

For the  $Z\gamma$  production, an effective theory with eight complex coupling parameters,  $h_i^V$ , where  $i = 1, 2, 3, 4$  and  $V = Z$  or  $\gamma$  [16] is introduced to describe the anomalous  $ZZ\gamma$  and  $Z\gamma\gamma$  couplings (see Fig. 10). A form factor with a common scale  $\Lambda$  is introduced to conserve tree-level unitarity at asymptotically high energies. The  $\Lambda = 1.2$  and 1.5 TeV are used to set the limits on  $CP$ -even coupling parameters  $h_{03}^V$  and  $h_{04}^V$ .

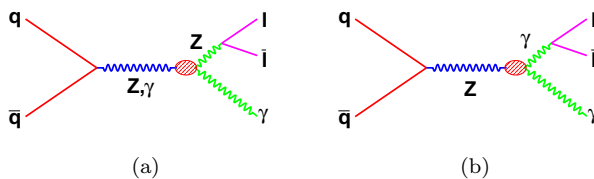


Figure 10: Feynman diagrams for the anomalous  $ZZ\gamma$  and  $Z\gamma\gamma$  couplings.

The contributions from anomalous couplings will increase the  $W\gamma$  and  $Z\gamma$  production cross section, and particularly give rise to an excess of photons in high transverse momentum. Thus, the photon transverse momentum distribution is used as the golden candle to search for anomalous departure from SM  $WW\gamma$ ,  $ZZ\gamma$  and  $Z\gamma\gamma$  couplings.

The photon  $p_T^\gamma$  distributions from  $W\gamma$  production is shown in Fig. 11, and used to derive limits on anomalous  $WW\gamma$  trilinear couplings using a binned likelihood fit to data. The 95% C.L. limits on the  $WW\gamma$  coupling parameters  $\Delta\kappa_\gamma$  and  $\lambda_\gamma$  are shown in Fig. 12, with the contour defining the two-dimensional exclusion limits. The one-dimensional 95% C.L. limits are  $-0.4 < \Delta\kappa_\gamma < 0.4$  and  $-0.08 < \lambda_\gamma < 0.07$ , which are obtained by setting one coupling parameter to the SM value and allowing the other to vary. These are the most stringent limits on anomalous  $WW\gamma$  couplings at a hadron collider.

The  $d\sigma/dp_T^\gamma$  distributions of  $Z\gamma$  production is shown in Fig. 13, and folded into a reconstruction-level distribution to derive the limits on anomalous coupling parameters  $h_{03}^V$  and  $h_{04}^V$ . To eliminate the FSR contribution, only events with  $p_T^\gamma > 30$  GeV and  $M_{ll\gamma} > 110$  GeV are considered. The 1D limits for  $\Lambda = 1.2$  TeV and 1.5 TeV are shown in Table 6, and the corresponding plots are

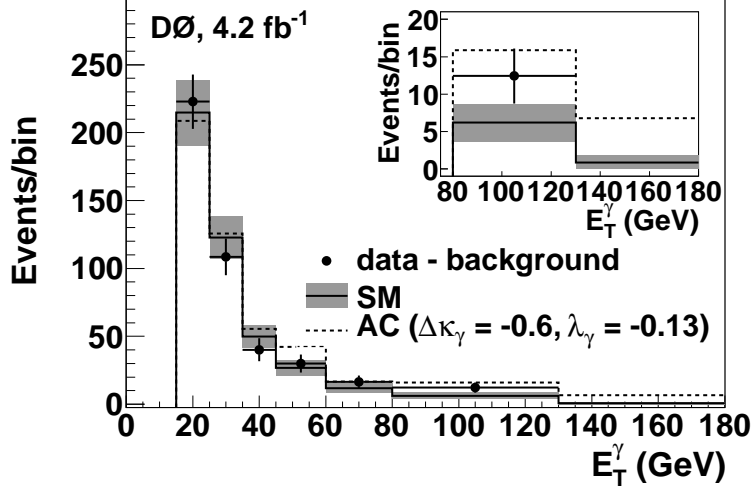


Figure 11: Photon transverse energy distributions for background-subtracted data compared to the expectation for the SM and for one choice of anomalous couplings for the combined electron and muon channels. The background-subtracted data are shown as black points with uncertainties representing the associated statistical and systematic uncertainties. The SM prediction is given by the solid line, with the shaded area representing its uncertainty. The effect of one example of anomalous couplings is represented by the dashed line. The last  $p_T^\gamma$  bin shows the sum of all events with  $p_T^\gamma > 130$  GeV. The inset shows the distributions in the last two bins of  $p_T^\gamma$ . (Figure from Ref. [1], see text)

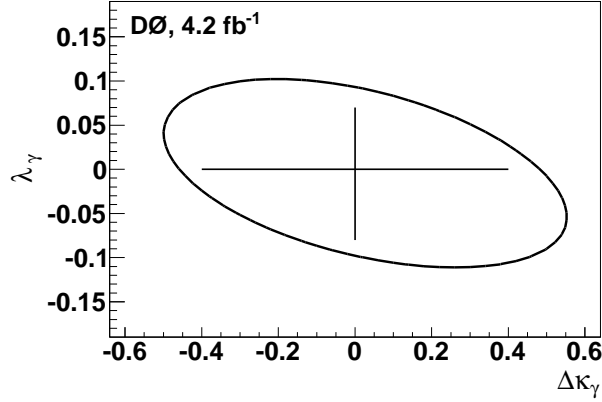


Figure 12: Limits on the  $WW\gamma$  coupling parameters  $\Delta\kappa_\gamma$  and  $\lambda_\gamma$ . The ellipse represents the two-dimensional 95% C.L. exclusion contour. The one-dimensional 95% C.L. limits are shown as the vertical and horizontal lines. (Figure from Ref. [1], see text)

shown in Figs. 14 and 15. After combining the previous  $1 \text{ fb}^{-1}$  D0  $Z\gamma$  analysis [17], the limits are shown in Fig. 16 and Table 6.

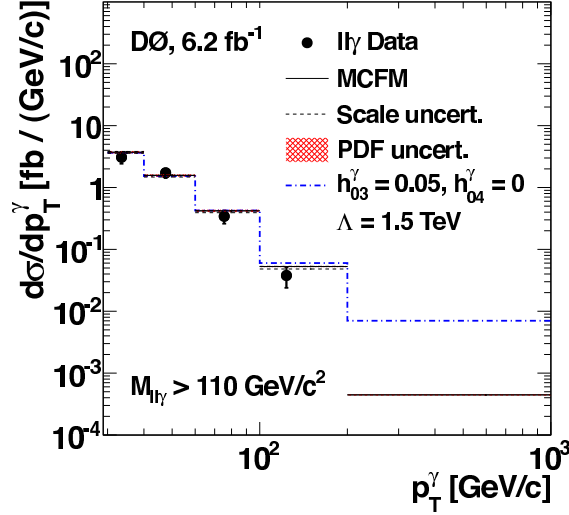


Figure 13: The SM prediction and anomalous  $Z\gamma$  coupling production compared with the unfolded  $d\sigma/dp_T^\gamma$  for combined muon and electron channels for  $p_T^\gamma > 30 \text{ GeV}$  and  $M_{ll\gamma} > 110 \text{ GeV}$ . (Figure from Ref. [2], see text)

Table 6: Summary of the 1D limits on the  $ZZ\gamma$  and  $Z\gamma\gamma$  coupling parameters at the 95% C.L. (Table from Ref. [2], see text)

	$ll\gamma \ 6.2 \text{ fb}^{-1}$		$ll\gamma \ 7.2 \text{ fb}^{-1}$
	$\Lambda = 1.2 \text{ TeV}$	$\Lambda = 1.5 \text{ TeV}$	$\nu\nu\gamma \ 3.6 \text{ fb}^{-1}$
			$\Lambda = 1.5 \text{ TeV}$
$ h_{03}^Z  <$	0.050	0.041	0.026
$ h_{04}^Z  <$	0.0033	0.0023	0.0013
$ h_{03}^\gamma  <$	0.052	0.044	0.027
$ h_{04}^\gamma  <$	0.0034	0.0023	0.0014

## 6 Conclusions and outlook

D0 has performed sophisticated studies of  $W\gamma$  and  $Z\gamma$  production using about half of the collected dataset. The results include the most precise measurements of the total production cross section of  $W\gamma \rightarrow l\nu\gamma$  and  $Z\gamma \rightarrow ll\gamma$ , and the first

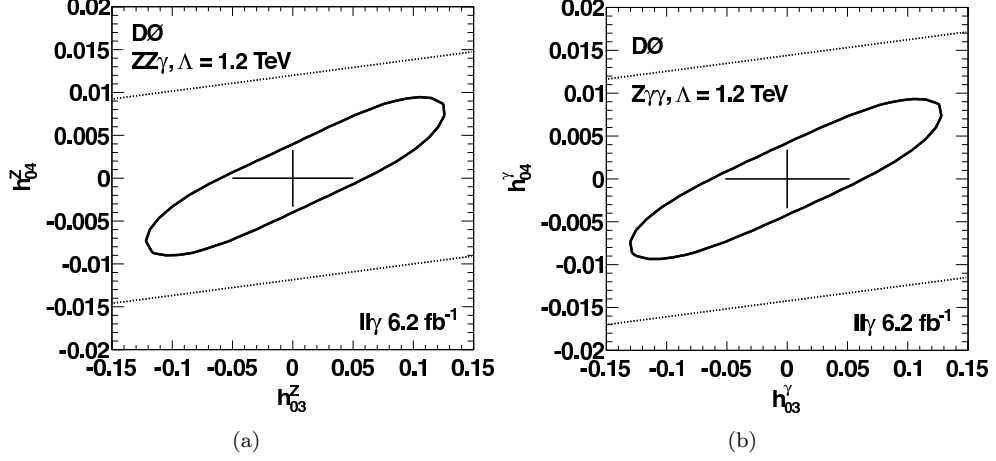


Figure 14: The 2D (contour) and 1D (cross) limits on the anomalous coupling parameters for (a)  $ZZ\gamma$  and (b)  $Z\gamma\gamma$  vertices at the 95% C.L. for  $\Lambda = 1.2$  TeV. Limits on  $S$ -matrix unitarity are represented by the dotted lines. (Figure from Ref. [2], see text)

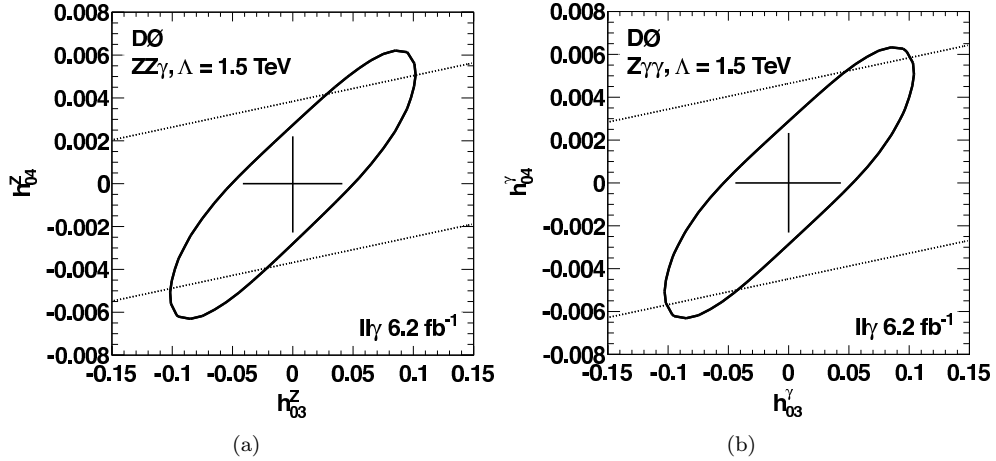


Figure 15: The 2D (contour) and 1D (cross) limits on the anomalous parameters for (a)  $ZZ\gamma$  and (b)  $Z\gamma\gamma$  vertices at the 95% C.L. for  $\Lambda = 1.5$  TeV. Limits on  $S$ -matrix unitarity are represented by the dotted lines. (Figure from Ref. [2], see text)

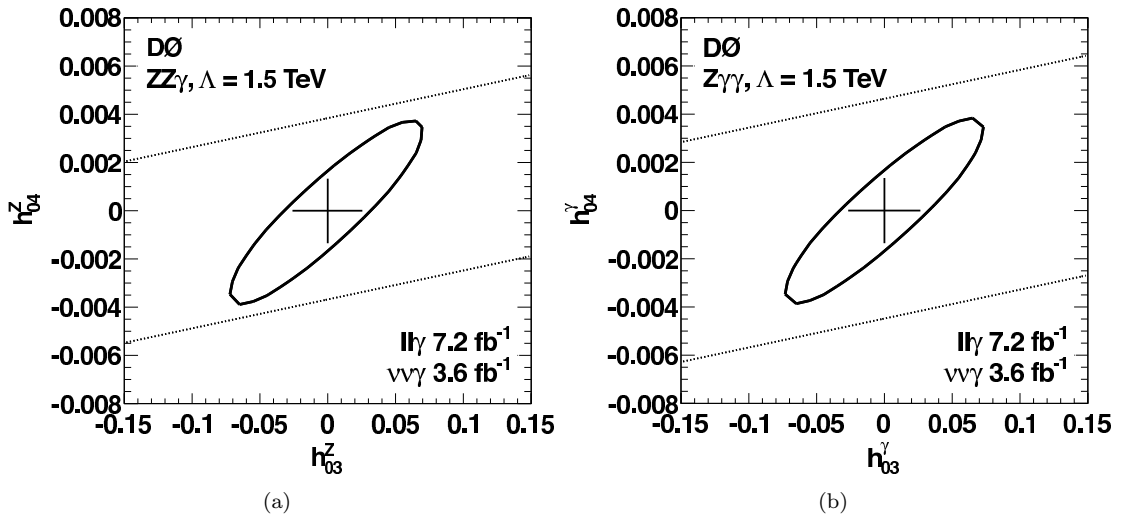


Figure 16: 2D (contour) and 1D (cross) limits on coupling parameters for (a)  $ZZ\gamma$  and (b)  $Z\gamma\gamma$  vertices at the 95% C.L. for  $\Lambda = 1.5$  TeV. Limits on  $S$ -matrix unitarity are represented by the dotted lines. (Figure from Ref. [2], see text)

unfolded photon differential cross section  $d\sigma/dp_T^\gamma$ , as well as the most stringent limits on the  $WW\gamma$  anomalous couplings. The D0 dataset will be continuously analyzed, and the high energy LHC experiments have already taken and analyzed data. The prospects for anomalous triple gauge boson couplings will be interesting and fruitful.

## References

- [1] V. M. Abazov *et al.* (D0 Collaboration), Phys. Rev. Lett. **107**, 241803 (2011).
- [2] V. M. Abazov *et al.* (D0 Collaboration), Phys. Rev. D **85**, 052001 (2011).
- [3] V. M. Abazov *et al.* (D0 Collaboration), Nucl. Instrum. Methods Phys. Res. A **565**, 463 (2006).
- [4] Pseudorapidity is defined as  $\eta = -\ln[\tan(\theta/2)]$ , where  $\theta$  is the polar angle relative to the proton beam direction.  $\phi$  is defined to be the azimuthal angle in the plane transverse to the proton beam direction.
- [5] K. O. Mikaelian, Phys. Rev. D **17**, 750 (1978); K. O. Mikaelian, M. A. Samuel, and D. Sahdev, Phys. Rev. Lett. **43**, 746 (1979); R. W. Brown, K. O. Mikaelian, and D. Sahdev, Phys. Rev. D **20**, 1164 (1979).
- [6] U. Baur, S. Errede and G. Landsberg, Phys. Rev. D **50**, 1917 (1994).

- [7] T. Sjöstrand *et al.*, JHEP **0605**, 026 (2006).
- [8] U. Baur, T. Han, J. Ohnemus, Phys. Rev. D **48**, 5140 (1993).
- [9] V. M. Abazov *et al.* (D0 collaboration), Phys. Rev. Lett. **102**, 231801 (2009).
- [10] V. M. Abazov *et al.* (D0 collaboration), Phys. Lett. B **690**, 108 (2010).
- [11] U. Baur and E. L. Berger, Phys. Rev. D **41**, 1476 (1990).
- [12] J. Pumplin *et al.*, J. High Energy Phys. **07**, 012 (2002); D. Stump *et al.*, J. High Energy Phys. **10**, 046 (2003).
- [13] R. Brun and F. Carminati, CERN Program Library Long Writeup W5013 (1993); we use GEANT version v3.21.
- [14] J. Campbell, R. Ellis, and C. Williams, J. High Energy Phys. **07** (2011) 018.
- [15] G. Bohm and G. Zech, *Introduction to Statistics and Measurement Analysis for Physicists* (Verlag Deutsches Elektronen-Synchrotron, Hamburg, 1998), ch. 9.
- [16] K. Hagiwara, R. Peccei, D. Zeppenfeld, and K. Hikasa, Nucl. Phys. B **282**, 253 (1987).
- [17] V. M. Abazov *et al.* (D0 Collaboration), Phys. Rev. Lett. **102**, 201802 (2009).